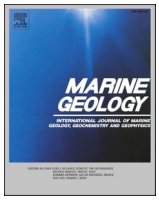
Marine Geology 491 (2026) 107662



Contents lists available at ScienceDirect

Marine Geology

journal homepage: www.elsevier.com/locate/margo



Research Article

Sedimentary dynamics in the subaqueous delta of the abandoned estuary: Effects of strong wave activity and riverine *re*-supply

Chaoran Lin [a], Longhai Zhu [a,b,*], Yaping Wang [c,d], Rui Bao [e], Rijun Hu [a,b], Lingpeng Meng [f]

[a] College of Marine Geo-Science, Ocean University of China, Qingdao 266100, China
[b] Key Lab of Submarine Geosciences and Prospecting Techniques, Ministry of Education, Ocean University of China, Qingdao 266100, China
[c] Ministry of Education Key Laboratory for Coast and Island Development, Nanjing University, Nanjing 210093, China
[d] State Key Laboratory of Estuarine and Coastal Research, East China Normal University, Shanghai 200241, China
[e] Frontiers Science Center for Deep Ocean Multispheres and Earth System, Key Laboratory of Marine Chemistry Theory and Technology, Ministry of Education, Ocean University of China, Qingdao 266100, China
[f] State Key Laboratory of Marine Geology, Tongji University, Shanghai 200092, China

ARTICLE INFO

Editor: N Senechal

Keywords:
Subaqueous delta
Abandoned estuary
High SSC
Sedimentary dynamics
Strong wave activity
Riverine re-supply

ABSTRACT

Global climate change and the decline in riverine sediment supply are profoundly reshaping the fate and trajectory of numerous river deltas around the world. Notably, subaqueous deltas of abandoned estuaries (SDAEs) resulting from river diversion represent an extreme example of zero riverine sediment supply, yet studies of these environments remain scarce. Based on in-situ bottom boundary layer observations in both spring and summer in the SDAE of the Yellow River, we examined the variation patterns and controlling mechanisms of sediment dynamics —under the effect of strong wave activity and the new secondary distribution. Strong wave events exhibited a pronounced dual influence on SSC; alongshore wave substantially increase SSC (>21.28 g/L) by enhancing sediment resuspension and liquefaction, whereas onshore wave significantly reduce nearshore SSC through water mass replacement (with values rapidly dropping from 13.11 g/L to 1.14 g/L). Riverine re-supply due to the new secondary course of the Yellow River has altered sediment transport pathways, enabling SSC in the SDAE to reach as high as 22.34 g/L under calm weather conditions, and resulting in a net alongshore sediment flux of 117 kg/m^2. We identified and established three conceptual models of fluid mud formation mechanisms: wave-supported, wave-current coupled fluid mud (WCFM), and river advection. We identified and established three conceptual models of fluid mud formation: wave-supported, wave-current coupled fluid mud (WCFM), and river advection. Identification of the WCFM highlights the sustained impact of strong wave activity on sediment transport within the SDAE. These findings advance our understanding of sediment dynamics in the SDAEs and provide valuable theoretical references and comparative examples for the studying the global evolution of abandoned or sediment-starved delta.

1. Introduction

Estuarine deltas, as crucial geomorphic interfaces between terrestrial runoff and the ocean, play vital roles in global sediment transport and coastal dynamics (Giosan et al., 2014; Darby et al., 2016; Nienhuis et al., 2020). However, under the intensifying pressures of global climate change and anthropogenic activities, the global fluvial sediment discharge exhibitd a widespread decline, causing most deltas to face severe erosion and retreat challenges, threatening their ecosystem stability and socioeconomic functions (Syvitski et al., 2009; Tessler et al., 2015; Wang et al., 2024). Hence, the subaqueous deltas of abandoned estuaries (SDAEs), which lose almost all of their fluvial sediment supply following river diversion, face further severe erosion. These areas are undergoing a transition from a sediment "sink" to a "source" (Schmidt et al., 2010; Shi et al., 2016), and represent the future evolutionary trajectory of deltas under conditions of extremely limited sediment supply (Nienhuis et al., 2013; Besset et al., 2019). Furthermore, amidst the pervasive decline in global fluvial sediment discharge, a growing number of deltas are experiencing a drastic reduction or even cessation of fluvial sediment supply. They are transforming into deltas of "abandoned" or "semi-abandoned" estuarine dominated by marine dynamics (Nienhuis et al., 2013; Besset et al., 2019; Yunus et al., 2022), exhibiting

* Corresponding author at: College of Marine Geo-Science, Ocean University of China, Qingdao 266100, China.
E-mail address: zhulonghai@ouc.edu.cn (L. Zhu).

https://doi.org/10.1016/j.margeo.2025.107662
Received 9 July 2025; Received in revised form 23 September 2025; Accepted 28 September 2025
Available online 8 October 2025
0025-3227/© 2025 Published by Elsevier B.V.

a sedimentary dynamic regime significantly different from that of active estuarine deltas (Chen et al., 2008a, 2008b; Liu et al., 2022; Zhu et al., 2024). Therefore, uncovering the sedimentary processes and sediment transport regulation mechanisms in such settings is of paramount theoretical importance for advancing our understanding of deltaic evolution under a diminished sediment supply on a global scale.

Sedimentary dynamics in estuarine deltas are inherently complex and driven by intricate interactions between river discharge, tidal currents, and wave action(Besset et al., 2019; Nienhuis et al., 2020). Collectively, these factors drive sediment erosion, transport, and deposition, exerting a critical influence on deltaic morphological evolution and material fluxes(Mentaschi et al., 2018; Caldwell et al., 2019). The suspended sediment concentration (SSC), a ubiquitous and critical agent of material transport and geomorphic modulation in estuarine deltas, profoundly influences sediment redistribution, landform evolution, pollutant migration, and organic carbon cycling (Weeks et al., 1993; Brand et al., 2010; Li et al., 2020). When the SSC exceeds a certain threshold (e.g., 3 g/L), it is typically referred to as High SSC. Under such conditions, not only are sediment settling and transport dynamics modified, but the ecological environment of the delta is also substantially altered, including intensified light attenuation and reduced primary productivity (Villaret and Trowbridge, 1991; Whitehouse, 2000; Tang et al., 2019). With further sustained increases in SSC, once a high concentration threshold (e.g., 10 g/L) is reached and the drainage rate of the water-sediment mixture falls below the net sediment input, the near-bed high SSC layer may transition into a fluid mud (FM) layer with distinct rheological properties (Ross and Mehta, 1989; Winterwerp, 1999; Liu et al., 2022; Tang et al., 2023), fundamentally restructuring sediment deposition and transport processes (Wu et al., 2023).

However, studies of High SSC and FM predominantly focused on active deltaic environments. In active deltas, the formation of High SSC and FM is typically governed by a suite of interacting factors, including strong wave (Ge et al., 2020; Liang et al., 2023), tidal currents (Becker et al., 2013; Qiu et al., 2017; Zhang et al., 2022), riverine sediment supply (Wu et al., 2015; Luo et al., 2022), extreme weather events (Fan et al., 2020, 2023), geomorphological features (Pelling et al., 2013), and anthropogenic modifications (Nicholls et al., 2020; Guan et al., 2022). The resulting patterns exhibited pronounced spatiotemporal heterogeneity. For example, in tide-dominated estuaries, high SSC and FM are generally maintained by sediment supply via tidal pumping (including tidal asymmetry and estuarine circulation) and are closely linked with stable maximum turbidity zones (Burchard et al., 2018; Becker et al., 2018; Li et al., 2023b; Wu et al., 2023; Zeng et al., 2024). By contrast, in river-dominated estuaries, high SSC and FM are primarily controlled by direct riverine sediment input (Bi et al., 2010; Becker et al., 2013; Wu et al., 2015; Li et al., 2023a).Despite the abundance of research on deltas in active estuaries, studies examining the formation mechanisms of High SSC and FM in SDAE remain scarce. This research gap hampers our understanding of the evolutionary trajectories of increasingly prevalent abandoned deltaic systems.

Following the 1996 avulsion, the SDAE of the Yellow River lost continuous sediment supply upstream and became dominated by marine dynamics. The maximum erosion depth exceeds 4 m, and the average annual erosion reaches 8.2×10^6 t, making this region one of the most intensely eroded and turbid among global deltas (Fan et al., 2020; Zhou et al., 2020; Liu et al., 2022). Additionally, frequent bifurcations at the mouth of the Yellow River periodically and indirectly supply sediment to this region through newly formed distributary channels. The coexistence of strong marine erosion and potential episodic riverine resupply creates a coupled hydrodynamic regime, rendering this region a natural laboratory for studying hydrodynamics–suspended sediment–seabed interactions and their evolution in the SDAE. Based on 24 days of bottom boundary layer tripod observations in spring and summer, we aimed to elucidate the variation characteristics of key sediment dynamic phenomena, including High SSC and FM, in the SDAE under the combined influence of strong wave activity and a new secondary distributary, and to further examine their controlling mechanisms and evolutionary patterns, which not only improves the understanding of sediment transport and evolutionary trends in the SDAEs but also provides a theoretical basis for their scientific management and ecological restoration.

2. Data and methods

2.1. Study area

The Yellow River Delta, a representative fluvial-dominated delta with a weak tidal influence, was once recognized globally as the fastest-growing and most dynamic estuarine delta. The modern Yellow River Delta is a massive fan-shaped accumulation that has developed since the river returned to the Bohai Sea in 1855 (Fig. 1b). During this period, the river mouth underwent 11 major avulsions, resulting in the formation of 5 large deltaic lobes (Zheng et al., 2018). Of them, the three deltaic lobes that formed prior to 1953 were reclaimed for construction and were no longer affected by marine dynamics. Contrastingly, the Shenxiangu–Diaokou (formed between 1953 and 1976) and Qingshuigou (formed since 1976) lobes continue to be subject to marine erosion. The Qingshuigou lobe itself consists of the Old-Qingshuigou sand spit (formed from 1976 to 1996), the Qing 8 sand spit (formed from 1996 to 2007), and the current river mouth, which was established since 2007 (Fig. 1a). Since the river mouth began discharging through the Qing 8 distributary channel in 1996, the subaqueous delta of the Old-Qingshuigou Estuary has been deprived of sediment supply and has transformed into a marine-dominated delta (Xing et al., 2016). The effect of the protruding sand spit of the Old-Qingshuigou resulted in a center of tidal high flow velocity at the front edge of the spit, with a measured maximum flow velocity of up to 1.7 m/s, and dominated by rectilinear current (Yang et al., 2021). Additionally, the coastal waters of the Yellow River Delta are strongly influenced by locally generated wind waves, whose heights are closely related to the wind speed. These waves exhibit rapid growth and dissipation, short periods, and marked seasonal variability. In the Yellow River delta, waves mainly originate from the east during spring and summer, and from the north during autumn and winter (Chen et al., 2008a, 2008b). Long-term wave observations in the Yellow River delta indicate a predominant wave direction of northeast, with waves of height < 0.5 m and 0.5–1.5 m occurring most frequently, accounting for 51.1 % and 36.3 % of the total, respectively. In contrast, large waves are comparatively rare, with 1.5–3 m waves and those exceeding 3 m comprising only 11.8 % and 0.5 % of occurrences, respectively. However, during seasonal extreme events such as cold surges and typhoons, strong waves can reach up to 4.2 m in height, often resulting in rapid and intense resuspension and dispersal of sediments in the Yellow River delta.

2.2. Data collection

Two sets of consecutive bottom boundary layer observations were conducted in the subaqueous delta of the Anandoned Estuary (Old QSG Estuary) of the Yellow River from March 28 to April 8, 2023 (11 days) and from August 17 to 30, 2024 (13 days). The observation locations are shown in Fig. 1c. All instruments were mounted on a stainless-steel tripod anchored to three pre-installed steel piles (5 m deep and 8 cm in diameter) driven into the seabed by divers to ensure stability throughout the observation period. The placement of the instruments on the tripod and the heights of the sensors above the seabed are illustrated in Fig. 1d and summarized in Table 1.

A downward-looking 6 MHz Nortek acoustic Doppler Velocimeter (ADV; measurement accuracy ±1 mm/s; data output rate 1–64 Hz) was used to measure near-bed flow velocity and direction. The ADV was sampled at 32 Hz, with 4096 measurements collected every 10 min. An upward-looking Teledyne RDI Acoustic Doppler Current Profilers (ADCP; measurement accuracy of ±0.5 %) measured velocity profiles from the top of the tripod to the surface, as well as wave time series, with

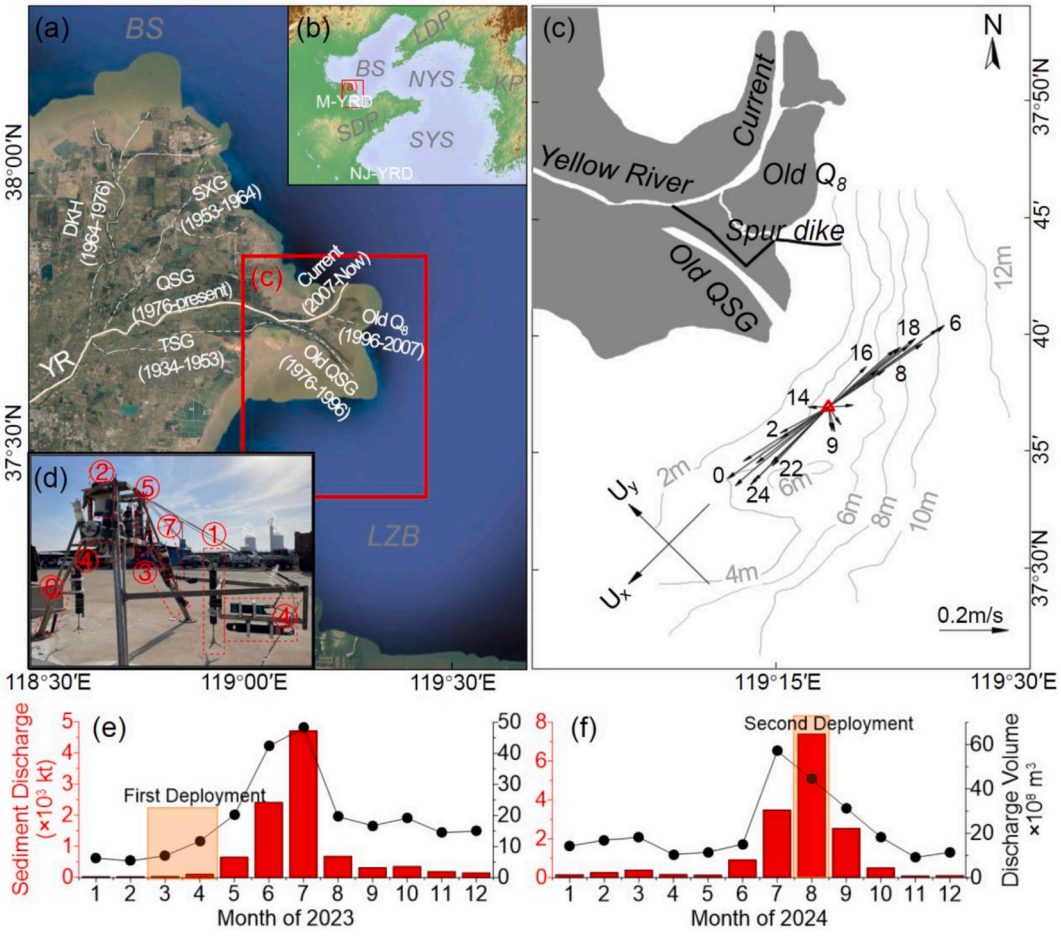


Fig. 1. (a) Location map of the modern Yellow River Delta; (b) Overview of the modern Yellow River Delta and changes in the channel leading to the sea; (c) The location and the current rose diagram of the observation station; (d) Bottom boundary layer observation system; (e) Monthly sediment discharge and discharge volume of the Yellow River in 2023; (f) Monthly sediment discharge and discharge volume of the Yellow River in 2024, the yellow-shaded area indicates the observation period. (LZB: Laizhou Bay; BS: Bohai Sea; NYS: North Yellow Sea; SYS: South Yellow Sea; SDP: Shandong Peninsula; LDP: Liaodong Peninsula; KP: Korean Peninsula; M-YRD: Modern Yellow River Delta; NJ-YRD: The Yellow River Delta in Northern Jiangsu; TSG: Tianshuigou; DKH: Diaokouhe; SXG: Shenxiangou; QSG: Qingshuigou; Old Q8: Old Qing 8). (For interpretation of the references to colour in this figure legend, the reader is referred to the web version of this article.)

Table 1
Deployed field instruments and their operational settings.

Serial number	Instruments	Height above the bed(cm)	Measured parameters	Burst intervals (s)	Sampling frequency (Hz)	Sampling numbers each burst
①	ADV	30[1]; 40[2]	Current	600	32	4096
②	ADCP	210[1], 200[2]	Wave, current	1200	/	/
③	310ty	30,60[1]; 20,90,160[2]	Turbidity	300	2	20
⑤	RBR-CTD	110[1]; 100[2]	Temperature, salinity	300	2	20
⑥	Tide gauge	20[1]; 10[2]	Tidal level	300	1	10
⑦	Sediment Trap	90[2]	Suspension sediment collection	/	/	/

[1] represents the height above the bed of the first deployment (March 28,2023-April 8, 2023);
[2] represents the height above the bed of the second deployment (August 18–30, 2024);

data collected every 20 min. A Haiying 1300 tide gauge (pressure accuracy ±0.3 kPa) was used to measure changes in water depth; the instrument sampled at 1 Hz, with measurements taken every 5 min. Three optical backscatter sensors (AQUAlogger310TY; turbidity accuracy ±0.2 % NTU) operated at a sampling frequency of 2 Hz, collecting 20 measurements every 5 min. A temperature-salinity-depth recorder (RBR XR420 CTD; temperature accuracy ±0.002 °C; conductivity accuracy ±0.003 mS/cm) measured temperature and salinity in the bottom boundary layer. The CTD was sampled at 2 Hz, with 20 data points recorded every 5 min. Additionally, during the summer deployment, a suspended sediment trap (diameter: 11 cm; length: 50 cm) was installed at 90 cmab to collect samples for subsequent SSC calibration. The sampling frequencies and sensor heights above the seabed for each instrument are listed in Table 1.

During the observation period, wind field data were derived from the 10 m near-surface wind speed product of ERA5, the fifth-generation global atmospheric reanalysis from the European Center for Medium-Range Weather Forecasts (ECMWF) (https://cds.climate.copernicus.eu/datasets), with a temporal resolution of 1 h and a spatial resolution of 0.25° × 0.25°.

2.3. ADV data quality control and calculation of wave

The data quality of each 10 min high-frequency burst measured by the ADV was assessed based on the acoustic signal correlation coefficient and signal-to-noise ratio (SNR). Data points with an SNR < 5 or correlation coefficient < 70 % were discarded; if more than 50 % of the data within a burst were excluded, the entire burst was removed. Subsequently, outliers were identified and removed using the phase space thresholding (PST) technique proposed by Goring and Nikora (2002).

During the April 2023 survey, the upward-looking ADCP did not successfully acquire wave data because of deployment issues. Therefore, wave parameters (including wave height and period) in April 2023 were extracted from the pressure and velocity records using the PUV (P: pressure; U: east velocity; V: north velocity) method (Wu, 1994; Sobey and Hughes, 1999; Gordon and Lohrmann, 2002). The wave orbital velocity (u_{br}) was determined by computing the contribution of each frequency component to the variance in the wave-induced bed velocity, followed by the inverse integration of $S_{uv,i}$.

$$u_{br} = \sqrt{2\Delta f \sum_i S_{uv,i}}$$

Where, $S_{uv} = S_{uu} + S_{vv}$ denotes the combined spectrum of the eastward (S_{uu}) and northward (S_{vv}) velocity components.

2.4. Estimation of bottom shear stress

Current-induced shear stress (τ_c), wave-induced shear stress (τ_w), and combined wave-current shear stress (τ_{cw}) were computed using the Grant-Madsen (GM79) model (Grant and Madsen, 1979). The detailed calculation procedures can be found in Grant and Madsen (1979). Required input parameters for the model include wave orbital velocity (u_{br}), wave frequency (ω), mean current velocity at height z_r ($\overline{u}_{cr}$), angle between wave and current ($\varnothing_{wc}$), and bed roughness (k_b). The u_{br} and ω were derived from PUV processing. The $\overline{u}_{cr}$ was obtained from the ADV measurements. The $\varnothing_{wc}$ was calculated as the difference between the dominant wave and current direction obtained from PUV analysis.The GM79 model provides estimates of the current-induced friction velocity (u_{*c}), the maximum wave-induced friction velocity (u_{*wm}), and the combined wave-current friction velocity (u_{*cw}). Subsequently, τ_c, τ_w and τ_{cw} were calculated using the following equations:

$$\tau_c = \rho_0 u_{*c}^2$$

$$\tau_w = \rho_0 u_{*wm}^2$$

$$\tau_{cw} = \rho_0 u_{*cw}^2$$

ρ_0 represents the fluid density, which was set to 1025 kg/m^3.

2.5. Analysis on sediment grain size and suspended sediment concentration

Here, sediment grain size was measured using an LS 13320 laser diffraction particle size analyzer (measurement range: 0.017–2000 μm; resolution: 0.1 φ). All samples were deflocculated piror to analysis. The grain size characteristics are shown in Fig. 2a. The sediments in the tripod area were classified as silty sand with a median grain size of 86.75 μm.

A total of 24 field water samples (1 L each) were collected during the deployment and retrieval of the tripod, with turbidity ranging from 4.90 to 896.33 NTU, which is considerably lower than those of the maximum turbidity values observed during the two field campaigns. Therefore, further laboratory calibration was performed using surface sediments collected near the observation station and suspended sediments collected from the tripod. In these experiments, 36 and 24,500-ml samples were prepared, with turbidity ranges of 100.65–3075.05 NTU and 7.95–2920.90 NTU. The calibration relationship between turbidity and SSC was established based on filtration experiments, and the calibration curves are shown in Fig. 2b, demonstrating a strong correlation between SSC and turbidity. Considering the vertical variations in suspended sediment grain size and related characteristics (Kineke and Sternberg, 1992; Wang et al., 2020), the calibration curves derived from the surface sediment experiments and developed with suspended sediments were applied to turbidity values measured by bottom turbidimeters (20, 30, and 60 cmab) and values from upper turbidimeters (90 and 160 cmab), respectively.

3. Results

3.1. Characteristics of tides, waves, and currents

The time series of the wind speed, wave parameters, current velocity, water depth, temperature, and salinity for both observation periods are presented in Figs. 3 and 4. Both observation periods were divided into four stages according to the wave conditions: micro-wave (F1, S1), pre-wind (F2, S2), strong-wave (F3, S3), and post-wind (F4, S4) stages. The

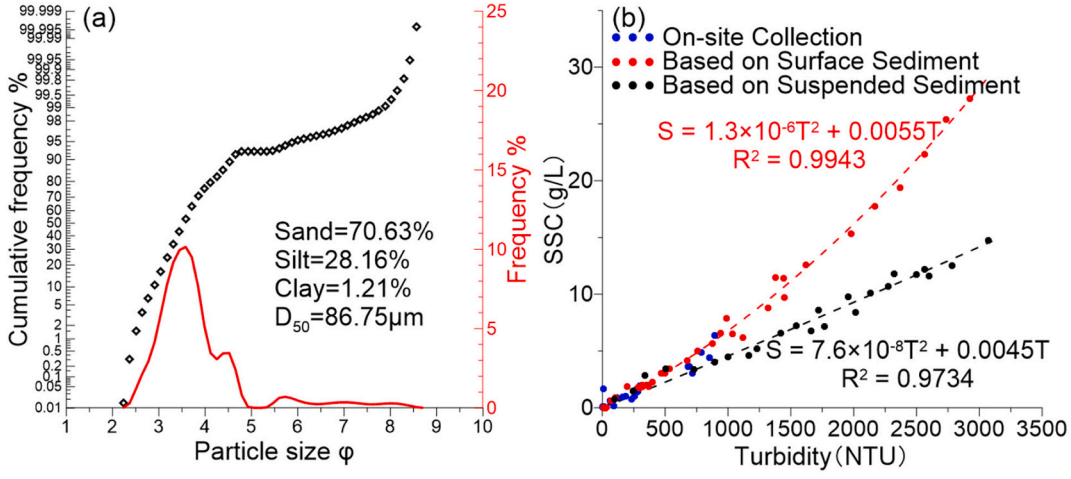


Fig. 2. (a) Surface sediment grain size characteristics at the observation station, the black and red curves indicate cumulative grain size and grain size distribution, respectively; (b) Calibration curves between turbidity (T: NTU) and SSC (S: g/L) obtained from laboratory experiments; the red, black and blue curves refer to surface sediments, suspended sediments, and field water samples, respectively. (For interpretation of the references to colour in this figure legend, the reader is referred to the web version of this article.)

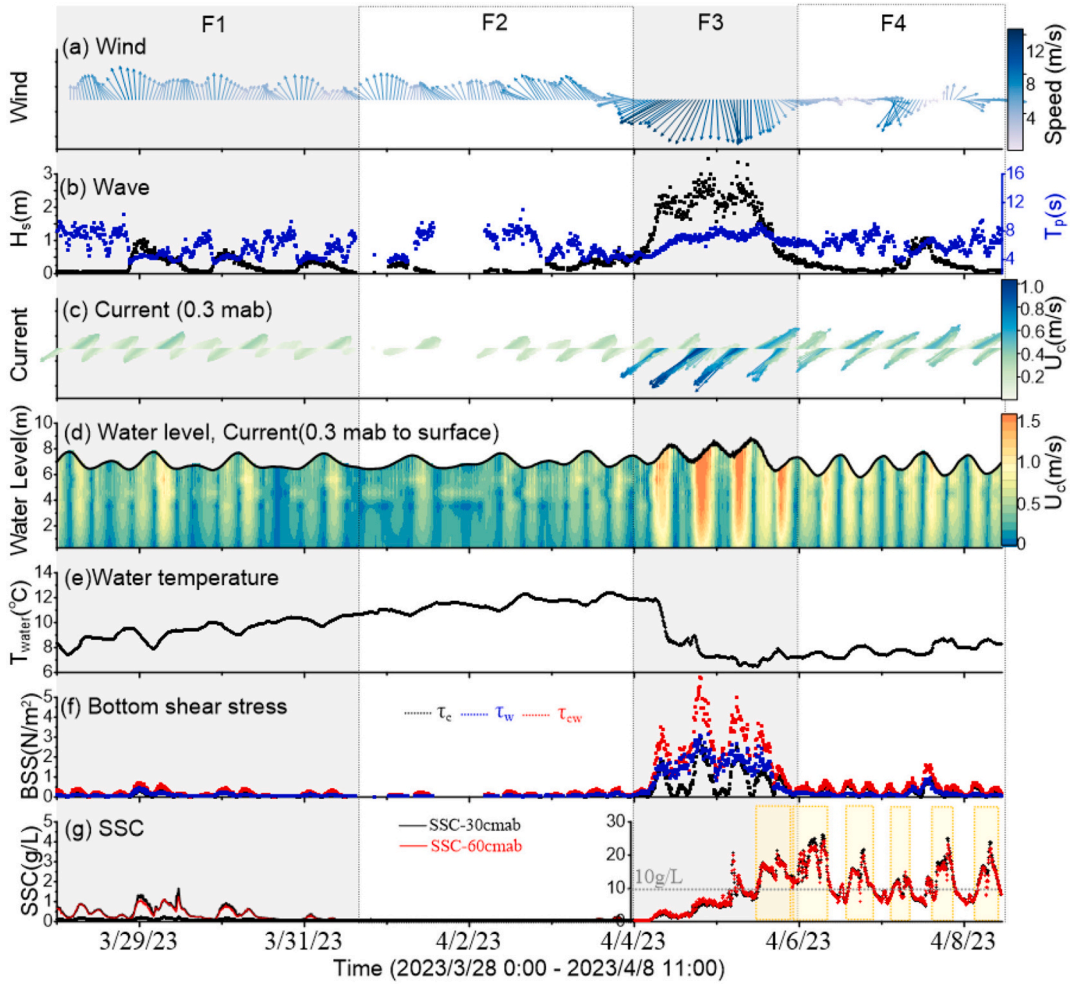


Fig. 3. Time-series of (a) wind, (b) wave (H_s and T_p: Significant wave height and period), (c) current in 0.3 mab (Uc: Current speed), (d) water level and current from 0.3 mab to surface layer, (e) water temperature, (f) bottom shear stress (τ_c: bottom shear stress due to currents, τ_w: bottom shear stress due to waves, τ_{cw}: bottom shear stress due to the combined currents and waves) and (g) SSC (SSC-30cmab: SSC at 30 cm from the bottom, SSC-60cmab: SSC at 60 cm from the bottom) during the period of field measurements (From March 28, 2023–0:00 to April 8, 2023–11:00). F1: Micro-wave Stage; F2: Pre-wind Stage; F3: Strong-wave Stage;F4: Post-wind stage. The (g) SSC was in a different vertical axis before and after 0:00 on April 4, 2023.

start and end times, as well as the maxima for each stage, are shown in Figs. 3, 4, and Table 2.

A pronounced strong wave event (defined as a significant wave height $H_S > 2$ m) was captured during both observation periods. During the strong-wave stage (F3) in spring, a maximum wind speed of 12.59 m/s from NNE was recorded (Fig. 3a). Under the influence of this strong wind, the H_S at the observation site peaked at 3.45 m, and waves with $H_S > 2$ m persisted for approximately 28 h (Fig. 3b). Similarly, during the strong wave stage (S3) in summer, a maximum wind speed of 14.72 m/s was recorded, and the dominant wind direction shifted from SE to SWW (Fig. 4a). During this period, the maximum H_S reached 2.67 m, and $H_S > 2$ m persisted for approximately 11 h (Fig. 4b). Apart from the strong wave stages (F3 and S3), the maximum H_S during the other stages was only 1.03 m, and the duration was relatively short (Figs. 3b and 4b).

During both observation periods, the tidal record at the observation site exhibited a distinct mixed semidiurnal tidal pattern, with maximum water levels of 8.75 m and 8.82 m, tidal ranges between 0.08 and 2.41 m and 0.2–1.88 m, and mean tidal ranges of 1.08 m and 1.22 m, respectively (Figs. 3d and 4d). The tidal currents in both periods were rectilinear, with flood tides flowing approximately southwest and ebb tides oriented northeast. During the first observation period, the maximum current velocity (1.04 m/s), maximum water depth (8.75 m), and largest tidal range (2.41 m) occurred during the strong wave event in the strong-wave stage (F3) (Figs. 3c and 4c). Contrastingly, during the second observation period, the maximum current velocity (1.09 m/s) was observed during the ebb tide in the pre-wind stage (S2), rather than that in the strong wave stage.

3.2. Bottom shear stress

Bottom shear stresses induced by tidal currents (τ_c), strong waves (τ_w), and their combined effect (τ_{cw}) during the two observation periods are presented in Figs. 3f and 4f. The maximum τ_c values were 2.95 N/m^2 (F3 stage) and 1.60 N/m^2 (S2 stage), respectively. The maximum τ_w values were 3.13 N/m^2 and 3.23 N/m^2, both occurring during the strong wave events in the strong-wave stages(F3, S3). During the non-strong wave stages, the temporal variations of τ_{cw} closely matched those of τ_c, indicating that tidal currents played a dominant role in bottom shear stress during these periods.

Contrastingly, significant differences in τ_{cw} patterns between the two observation periods were observed during the strong wave stages. During the strong wave event in the strong-wave stage (F3), τ_{cw} was influenced by both the substantially increased τ_c and τ_w, reaching a maximum of 5.99 N/m^2, and the highest values coincided with the maximum current velocity. Contrastingly, during the strong wave event of the strong-wave stage (S3), τ_c varied only slightly (maximum 1.04 N/m^2), τ_{cw} was mainly governed by τ_w and closely followed its trend, with a maximum of just 3.55 N/m^2, which was significantly lower than that in

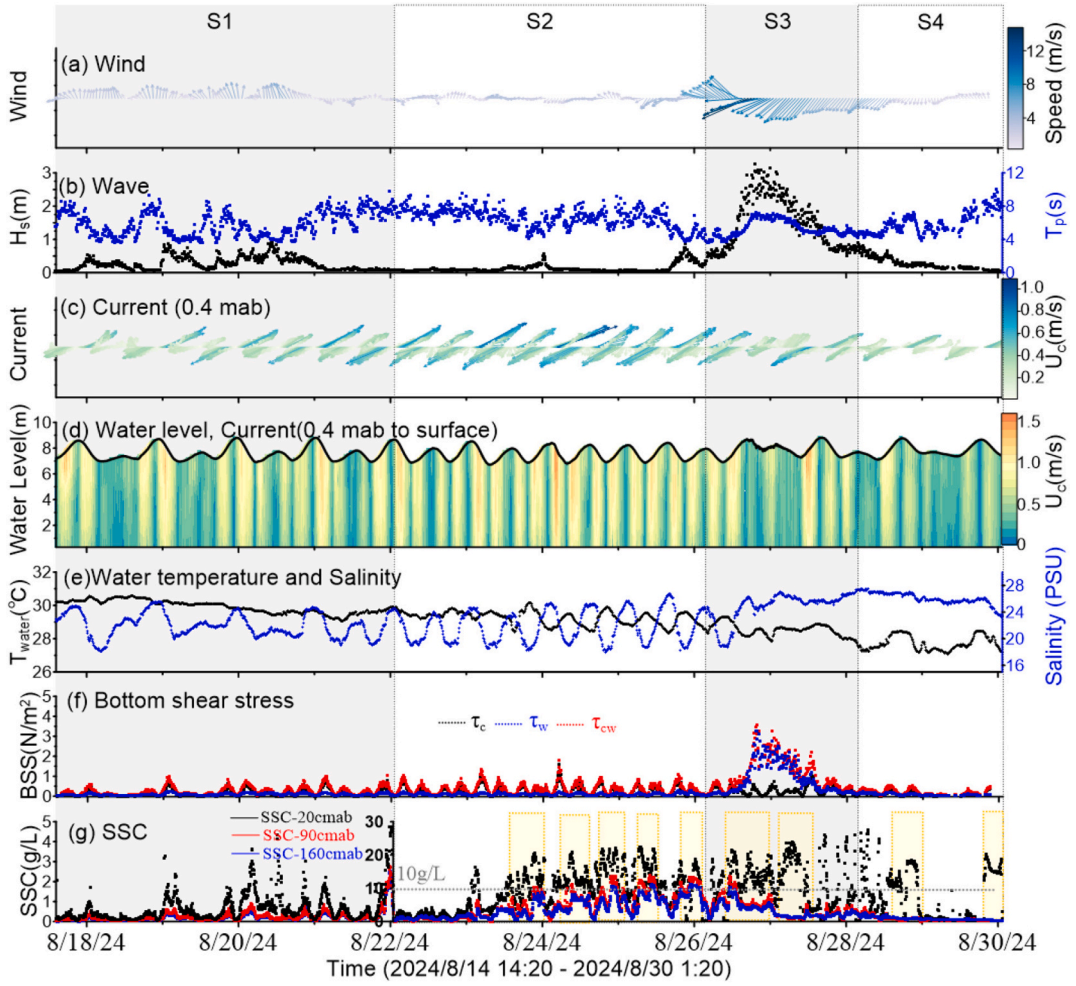


Fig. 4. Time-series of (a) wind, (b) wave (H_s and T_p: Significant wave height and period), (c) current in 0.4 mab (Uc: Current speed), (d) water level and current from 0.4 mab to surface layer, (e) water temperature and Salinity, (f) bottom shear stress (τ_c: bottom shear stress due to currents, τ_w: bottom shear stress due to waves, τ_{cw}: bottom shear stress due to the combined currents and waves) and (g) SSC (SSC - 20,90,160 cmab: SSC at 20, 90, and 160 cm from the bottom) during the period of field measurements (From August 17, 2024–14:20 to August 30, 2024–1:20). S1: Micro-wave Stage; S2: Pre-wind Stage; S3: Strong-wave Stage; S4: Post-wind stage. The (g) SSC was in a different vertical axis before and after 1:00 on August 22, 2024.

Table 2
Maximum value statistics for each stage.

	Spring				Summer			
	F1	F2	F3	F4	S1	S2	S3	S4
Depth (m)	7.73	7.79	8.84	7.71	8.82	8.68	8.83	8.78
Current (m/s)	0.45	0.36	1.04	0.61	0.78	1.09	0.75	0.56
Hs (m)	1.03	0.78	3.45	1.08	1.00	0.87	3.24	0.88
τ_c(N/m^2)	0.41	0.25	2.95	0.83	0.84	1.60	1.04	0.43
τ_w(N/m^2)	0.42	0.23	3.13	0.92	0.23	0.27	3.23	0.20
τ_{cw}(N/m^2)	0.69	0.43	5.99	1.57	1.01	1.79	3.55	0.54
SSC-30cmab (g/L)	1.68	0.31	21.28	25.99	/	/	/	/
SSC-60cmab (g/L)	1.28	0.24	20.33	24.20	/	/	/	/
SSC-20cmab (g/L)	/	/	/	/	9.27	22.34	25.82	27.32
SSC-90cmab (g/L)	/	/	/	/	2.76	13.95	13.57	4.38
SSC-160cmab (g/L)	/	/	/	/	2.52	10.93	10.15	2.38

the strong-wave stage (F3).

3.3. High SSC and FM

Temporal variations in the SSC within the bottom boundary layer during both observation periods are illustrated in Figs. 3g and 4g. During the spring observation period, the SSC ranged from 0 to 25.99 g/L. High SSC was observed primarily during the strong wave period in the strong-wave stage (F3) and the subsequent post-wind stage (F4), with mean SSC of 6.88 g/L and 12.05 g/L, respectively. Furthermore, driven by strong waves, SSC increased progressively with wave duration. The maximum value (25.99 g/L) occurred under calm sea conditions immediately following the peak wave, rather than coinciding with the maximum τ_w. During the micro-wave stage (F1), under the influence of relatively small waves (Hs < 0.5 m), the SSC exhibited only minor fluctuations with wave height and current velocity, with a maximum

value of just 1.68 g/L. Under calm conditions during the pre-wind stage (F2), the SSC exhibited almost no variation and remained at a persistently low level with an average of 0.04 g/L. Additionally, SSC at 30 and 60 cmab displayed almost identical temporal variation patterns during the spring observation period.

During the summer observation period, the variation pattern of the SSC differed substantially from that of the spring observations, as a High SSC was evident during the pre-wind (S2), strong-wave (S3), and post-wind (S4) stages. During the pre-wind stage (S2), the SSC remained at a relatively high with an average value of 5.78 g/L. Despite the mean τ_cw increasing by only 0.12 N/m^2 compared with that in the micro-wave stage (S1), SSC exhibited an almost thirtyfold increase (Fig. 4f, g). Furthermore, during the strong-wave stage (S3), the SSC at 20, 90, and 160 cmab exhibited markedly different variation trends. In the initial phase of the strong-wave stage (S3), SSC at all three elevations showed a decreasing trend; however, the reduction in SSC at 20 cmab was markedly less than that observed at 90 and 160 cmab. During the later phase of the strong-wave stage (S3) and throughout the post-wind stage (S4), the SSC at 20 cmab exhibits several pronounced increases, reaching a maximum value of 27.32 g/L. Contrastingly, SSC at 90 and 160 cmab remained at consistently low levels, with average values of 0.89 g/L and 0.64 g/L, respectively.

Using SSC >10 g/L as the threshold for FM formation (Tang et al., 2023; Wu et al., 2023), FM appeared during all stages except for the micro-wave stage in both the spring and summer observation periods. In spring, FM development was closely linked to strong wave processes (Fig. 3g). FM was primarily observed in the later part of the strong-wave stage (F3), persisted under calm conditions at the onset of the post-wind stage (F4), and reached its peak value. Furthermore, during the subsequent post-wind stage (F4), the FM exhibited a vertical thickness greater than 60 cm and a periodic development pattern. In contrast to spring, FM developed mainly in the pre-wind stage (S2) during summer (Fig. 4g). The development of the FM during this stage was closely associated with the abnormal increase in SSC resulting from the river resupply event observed during the summer observation period (see Section 4.2). However, at the onset of the strong-wave process in S3, despite the intensified hydrodynamic forcing, the development of the FM was reduced.

4. Discussion

4.1. High Suspended sediment concentration controlled by strong waves

The impact of the strong-wave on the High SSC was most pronounced during both observation periods. During the strong-wave stages (F3 and S3), the near-bottom SSC increased by approximately 30 times compared with that in the micro-wave stage (F1, S1), with maximum values of 21.28 and 25.82 g/L, respectively (Figs. 3g and 4g). During this period, the maximum τ_{cw} ranged from 3.50 to 5.98 N/m^2 and from 2.27 to 3.55 N/m^2 (Figs. 3f and 4f), which far exceeded the critical erosion shear stress of 0.2 N/m^2 for sediments in this region (Lin et al., 2024). The substantial increase in τ_{cw} effectively overcame the critical erosion shear stress, thereby triggering intense sediment resuspension and providing ample sediment supply for the formation of High SSC. Contrastingly, although sediment resuspension occurred under excessive shear stress during the micro-wave stage (F1 and S1), both its intensity and SSC were significantly lower than those during the strong-wave stage (F3 and S3) (Figs. 3 g and 4 g). This also indicates that strong waves are the primary driving force for the formation of High SSC in the SDAE of the Yellow River (Qiu et al., 2017; Liu et al., 2020; Niu et al., 2020).

During strong wave events in the F3 stage, near-bed SSC substantially exceeded the lower threshold for FM, exhibiting characteristics similar to classic wave-supported fluid mud (WSFM), which is typically characterized by rapid formation under intense wave forcing and quick dissipation once wave energy diminishes (Hale and Ogston, 2015; Liu et al., 2022). However, unlike classic WSFM, the FM observed during the F3 stage not only persisted throughout the strong wave conditions but also showed notable continuity and accumulation, continuing to develop even after wave activity ceased (Figs. 3g). SSC displayed a distinct gradual accumulation pattern, with its peak occurring not during periods of maximum wave height or peak τ_{cw}, but rather during calm conditions following the wave subsidence. This behavior contrasts with predictions from existing sediment transport models, which generally indicate a positive correlation between SSC and bottom shear stress (Brand et al., 2010; Liu et al., 2020). The asynchronous response of SSC and FM to hydrodynamic forcing suggest that, in addition to sediment resuspension driven by τ_{cw} during strong-wave events, other critical sediment dynamic processes contribute to SSC variations.

Grain size analysis indicated that the surface sediment in the study area was silty sand (Fig. 2a). Earlier studies showed that silty sediments are susceptible to liquefaction under cyclic wave loadings (Fettweis et al., 2010; Jia et al., 2014). However, this study lacked direct observations, such as pore water pressure data, to directly confirm the occurrence of liquefaction. However, observations from Liu et al. (2020) in the northern Yellow River subaqueous delta revealed that, during a strong-wave event with a significant wave height of 3 m, the sediment liquefaction ratios at 30 cm and 60 cm beneath the bed reached 80 % and 65 %, respectively. Therefore, based on the comparable duration, wave height, and sediment characteristics during the strong-wave stage (F3), we inferred that significant bed liquefaction likely occurred during this period. Furthermore, as wave-induced sediment liquefaction is a progressive process (Jia et al., 2014), the SSC increases at the onset of the strong-wave process, which is mainly attributed to wave-induced resuspension. This accounts for the relatively low SSC of 7 g/L at the maximum τ_{cw} in the strong-wave stage (F3) (Fig. 3g). As the wave action persisted, the accumulation of sediment pore pressure intensified bed liquefaction and progressively reduced the shear strength of the sediment. Consequently, even tidal currents alone can induce strong resuspension, leading to a further marked increase in SSC (approximately 20 g/L). This finding suggests that the contribution of wave-induced bed liquefaction to high SSC may exceed that of bottom shear stress induced sediment resuspension.

Compared with those in the F3 stage, the hydrodynamics and SSC variation during the strong-wave process in the S3 stage exhibited significant differences, primarily due to differences in wind direction. The principal tidal constituents (O_1, P_1, K_1, N_2, M_2, and S_2) were considered, and harmonic analysis using the T-TIDE toolbox (Pawlowicz et al., 2002) was applied to the observed water depth, Ux (current velocity parallel to the isobath, positive to the NE), and Uy (current velocity perpendicular to the isobath, positive to the NW) to analyze variations in water depth and current velocity during the strong-wave process. Fig. 5 presents a comparison between the harmonic analysis (harmonic value) and the observed (observed value) results.

On short time scales, wind serves as a critical factor that can force lateral water movement (Llebot et al., 2014; Liang et al., 2023). During the strong-wave stage (F3), the wave direction was generally aligned with the flood current, and the combined effect of waves and tidal currents produced marked increases in alongshore Ux (SW direction) and onshore Uy (NW direction), with average increases of 0.36 m/s and 0.09 m/s, respectively; the maximum increase in flood current velocity was 0.36–0.53 m/s (Fig. 5c-e). Consequently, the hydrodynamic forcing during this stage was intense and vertical mixing was uniform. SSC was primarily affected by resuspension from τ_{cw} in the early strong-wave period, while in the late period, bed liquefaction induced by wave cyclic loading likely played the dominant role.

During the strong-wave stage (S3), the wave direction shifted from NE to SW and became oblique to the tidal flow, resulting in a misalignment between the wind-driven and tidal currents. The alongshore Ux (NE direction) and offshore Uy (SE direction) both slightly decreased, with average reductions of 0.14 m/s and 0.12 m/s, respectively (Fig. 5c-e). The wind-driven flow forced low SSC water from a

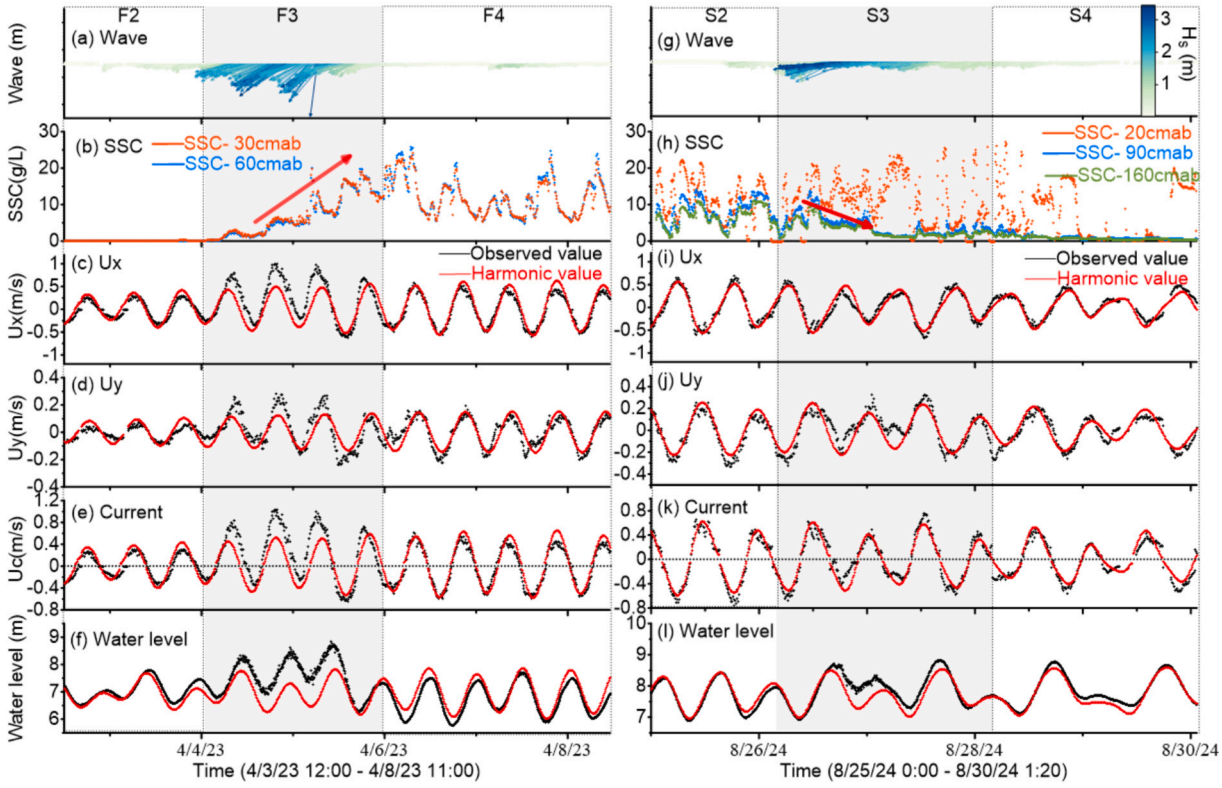


Fig. 5. Time-series of (a, g) wave; (b, h) SSC; (c, i) Ux (velocity parallel to isobaths, positive in the SW direction); (d,j) Uy (velocity perpendicular to isobaths, positive in the NW direction); (e,k) Current; (f, i)Water level,during the strong-wave period. The black and red lines denote observed values and harmonic values, respectively. a-d: From April, 3–0:00 to April 8, 2023–11:00; From August 25, 2024–0:00 to August 30, 2024–1:20. (For interpretation of the references to colour in this figure legend, the reader is referred to the web version of this article.)

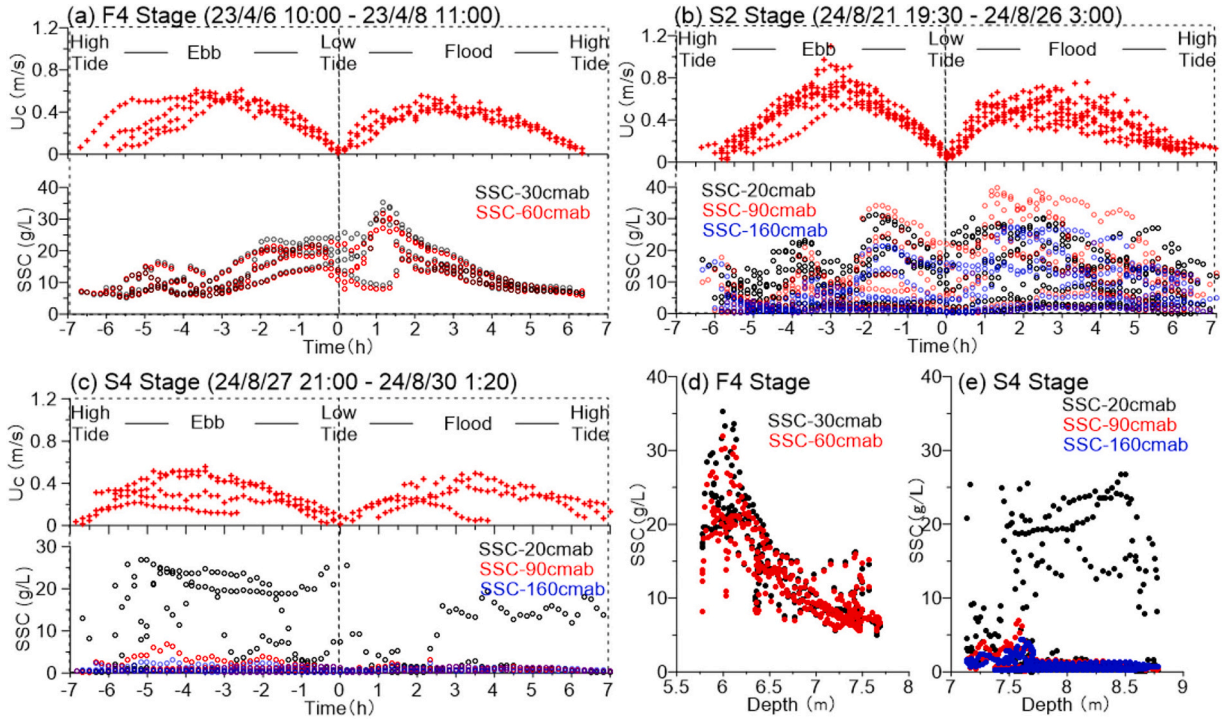


Fig. 6. (a–c) Variations of Uc and SSC during flood and ebb tides in the F4, S2, and S4 stages (with zero on the x-axis indicating low tide); (d, e) Scatter plots of water depth versus SSC in the F4 and S4 stages.

distant NE offshore area into the observation site, causing water mass replacement and a remarkable decrease in SSC at the site. Thus, in the early phase of the strong-wave stage (S3), when bottom shear stress rapidly increased, SSC at both 90 and 160 cmab decreased remarkably from 13.11 g/L to 1.14 g/L (Fig. 5h). The significant increase in seawater salinity at the onset of the strong-wave stage (S3) further supports the intrusion of offshore water (Fig. 4e). In the late phase of the strong-wave process, enhanced sediment resuspension caused by large τ_{cw} resulted in a significant increase in SSC at 20 cmab, rising to 25 g/L, whereas SSC at 90 and 160 cmab remained low (<10 g/L), indicating inadequate vertical mixing and the formation of marked turbidity stratification near the seabed (Fig. 5h).

Furthermore, several episodes of high SSC and FM were recorded under calm conditions following strong wave events during the F4 and S4 stages. No substantial wave activity was observed during these intervals, indicating that the high SSC and FM were not directly sustained by wave action. Additionally, during this period, SSC and FM levels showed a positive correlation with tidal current direction and a pronounced negative correlation with water depth, occurring predominantly during ebb and low tide stages (Fig. 6a and c-e). These patterns suggest that the high SSC and FM observed during this stage were supplied through advective transport from other region rather than generated by local resuspension. This phenomenon may result from intensified wave-induced erosion in nearshore areas during earlier strong wave events. Due to shallower water depths and stronger wave dynamics in nearshore zones compared to the observation site, these regions experience enhanced wave-driven erosion and sediment resuspension (Grant and Madsen, 1979; Egan et al., 2019). The remobilized sediments are subsequently transported to the observation site via ebb currents and gravity-driven processes. Accordingly, this study designates such FM, primarily sourced from nearshore wave-induced erosion and delivered to the observation site through tidal pumping and gravity-driven secondary transport, as "wave–current coupled fluid mud (WCFM)", emphasizing the coupled mechanisms of wave-induced erosion and current-mediated sediment transport involved in its formation.

4.2. Influence of new secondary distributary

In addition to the impact of strong-wave events, the pre-wind stage (S2) also exhibited an anomalous increase in SSC with a peak of 22.34 g/L, and the SSC at all three heights remained above 10 g/L during the mid-to-late period of the S2 stage (Fig. 4g). Compared with that of the micro wave stage (S1), the SSC increased by nearly one order of magnitude, whereas the current velocity only increased by 0.3 m/s. This pronounced decoupling between the hydrodynamic intensity and SSC variations suggests that, in addition to sediment resuspension, other sources of SSC may exist during the S2 stage. Remote sensing image analysis strongly supports this inference. Fig. 7 (a and b) shows Sentinel images of the study area during the observation period, downloaded via the Google Earth Engine (https://code.earthengine.google.com) and processed using standard false-colour composites. The images clearly show that the sediment concentration in the Yellow River estuary and plume on August 28, 2024, was significantly higher than that on April 1, 2023 (Fig. 7a-b). A new secondary distributary channel emerged in 2018, located south of the current estuary and north of the Old-QSG Estuary, which significantly changed the sediment transport pathways of the Yellow River into the sea (Fig. 7a-b).

Over the 28-year period following the 1996 course shift of the Yellow River and prior to the emergence of the secondary distributary channel, Yellow River sediment was discharged into the sea through the northern estuary. Due to the influence of shear fronts and tidal currents, the subaqueous delta of the Old-QSG estuary receives little sediment from the Yellow River (Gao et al., 2016; Wang et al., 2017). The new secondary distributary channel significantly changed the sediment transport pathways of the Yellow River, enabling riverine sediments to reach

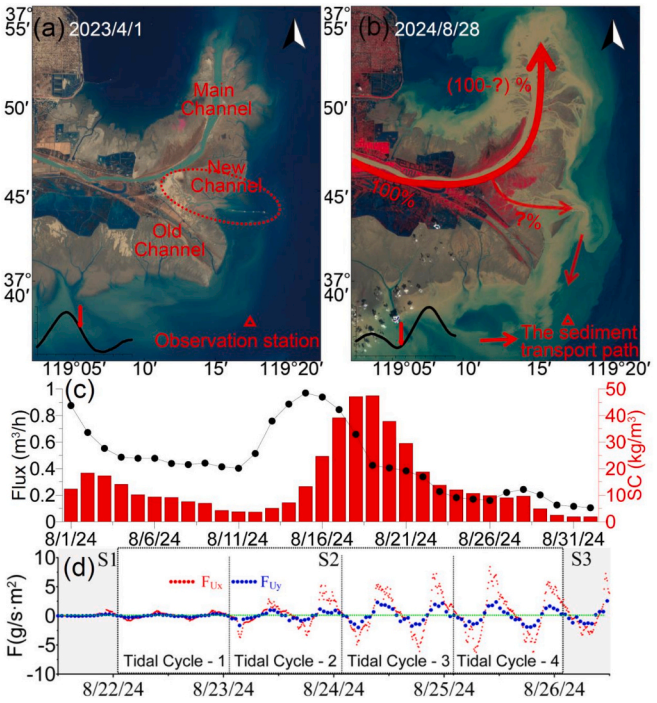


Fig. 7. (a) Remote sensing image acquired on April 1, 2023, and (b) on August 28, 2024; (c) Daily variations of water flux and sediment concentration at Lijin Station in August, The red curve in the lower left corner represents the water level change on that day, and the arrows indicate the time when the remote sensing image images were obtained.; (d) Time series of suspended sediment transport fluxes. F_{Ux} and F_{Uy} represents alongshore (positive to the southwest, negative to the northeast) and F_{Uy} onshore (positive onshore, negative offshore) suspended sediment fluxes, respectively. (For interpretation of the references to colour in this figure legend, the reader is referred to the web version of this article.)

the deltaic region more easily during flood tide events. Additionally, hydrological data from the Lijin Station of the Yellow River (www.yrcc.gov.cn) indicated that a water-sediment regulation event occurred in mid-August 2024, resulting in approximately 5 days of elevated river discharge and sediment load (Fig. 7c). This event was temporally consistent with that of the anomalous increase in the SSC observed at the monitoring site. Fig. 7d presents the suspended sediment flux during S2 stage (based on SSC-90 cmab), where F_{Ux} and F_{Uy} denote the alongshore (positive southwestward, negative northeastward) and cross-shore (positive onshore, negative offshore) suspended sediment fluxes, respectively. When F_{Ux} is positive, the SDAE of the Yellow River receives the sediment supply delivered by advection. As shown in Fig. 7d, F_{Ux} increased markedly during the second tidal cycle of S2 stage, with a peak value of 5.22 g/s m^2. In the following two tidal cycles, the maximum F_{Ux} values were 7.23 g/s m^2 and 8.42 g/s m^2, and the absolute value of F_{Ux} during flood tides was consistently much greater than that during ebb tides. During the four tidal cycles in S2 stage, the net alongshore sediment flux was approximately 117 kg/m^2, indicating that the SDAE received a substantial amount of Yellow River sediment due to the combined effects of the new secondary distributary channel and advection.

Furthermore, during the S2 stage, FM developed even in the absence of either direct or indirect wave influence. As discussed above, sediment replenishment from the new secondary distributary channel, combined with advective transport, predominantly controlled SSC variability during this stage, A pronounced tidal cycle was observed, with SSC during flood tides significantly higher than during ebb tides (Fig. 6b). Based on this, we infer that the high SSC and FM observed during the S2 stage resulted from a combination of sediment supply from the new

secondary distributary channel and northward transport driven by flood-tide advection to the observation site, providing both the material source and the transport mechanism for FM development. This type of FM—driven by riverine sediment input and formed through tidal advective transport—is designated as "riverine-advected fluid mud (RAFM)", underscoring the co-dominant roles of riverine input and tidal advection in its formation.

4.3. Sedimentary dynamics in the subaqueous delta of the abandoned estuary and compared with other deltas

As discussed above, the SDAE of the Yellow River exhibits significant complexity and coupling in sedimentary dynamic processes, including high SSC and FM, under varying hydrodynamic regimes. These dynamics are regulated by the combined influences of tidal currents, waves, wind-driven flows, and periodic riverine resupply. Accordingly, we propose a conceptual model of sedimentary dynamics for the SDAE (Fig. 8a), illustrating how, in the context of river diversion, intense marine forcing and episodic riverine resupply interact to govern sedimentary processes in this region, mechanisms that are widely observed across deltaic environments globally (Nienhuis et al., 2013; Mentaschi et al., 2018; Chadwick et al., 2022).

Strong wave events are fundamental natural agents in shaping deltaic morphology and controlling SSC dynamics in estuarine environments (Giosan et al., 2014; Nienhuis et al., 2020; Yao et al., 2024). Unlike conventional coastlines, subaqueous deltas exhibit heightened sensitivity and responsiveness to wave energy due to their ralatively shallow water depths and gentle slopes (Chen et al., 2008a, 2008b). However, our findings reveal a pronounced duality in the effects of strong wave events on SSC, strongly modulated by wind direction. Notably, under intense alongshore wave conditions (such as during F3), nearshore SSC increases significantly due to enhanced sediment resuspension and bed liquefaction (Fig. 8b). This phenomenon aligns with observations from major wave-dominated deltas—including the Mississippi (Hou et al., 2024) and Ganges-Brahmaputra (Yunus et al., 2022)—where strong waves serve as the primary driver of sediment dynamics, sustaining high SSC levels even as fluvial sediment supply declines. In contrast, during onshore wind-wave events (such as during S3), although high shear stress is generated, wind-driven current induced water mass replacement at the onset of the event can reduce SSC levels (Fig. 8c). Such wind direction–controlled water mass replacement is common in shallow, low-gradient coastal systems, yet it has seldom been addressed in deltaic research, which often emphasizes direct wave-induced resuspension (Baeye et al., 2011; Aleskerova et al., 2019; Colosimo et al., 2020). This duality in wave influence under varying wind directions offers novel insights into sediment dynamics

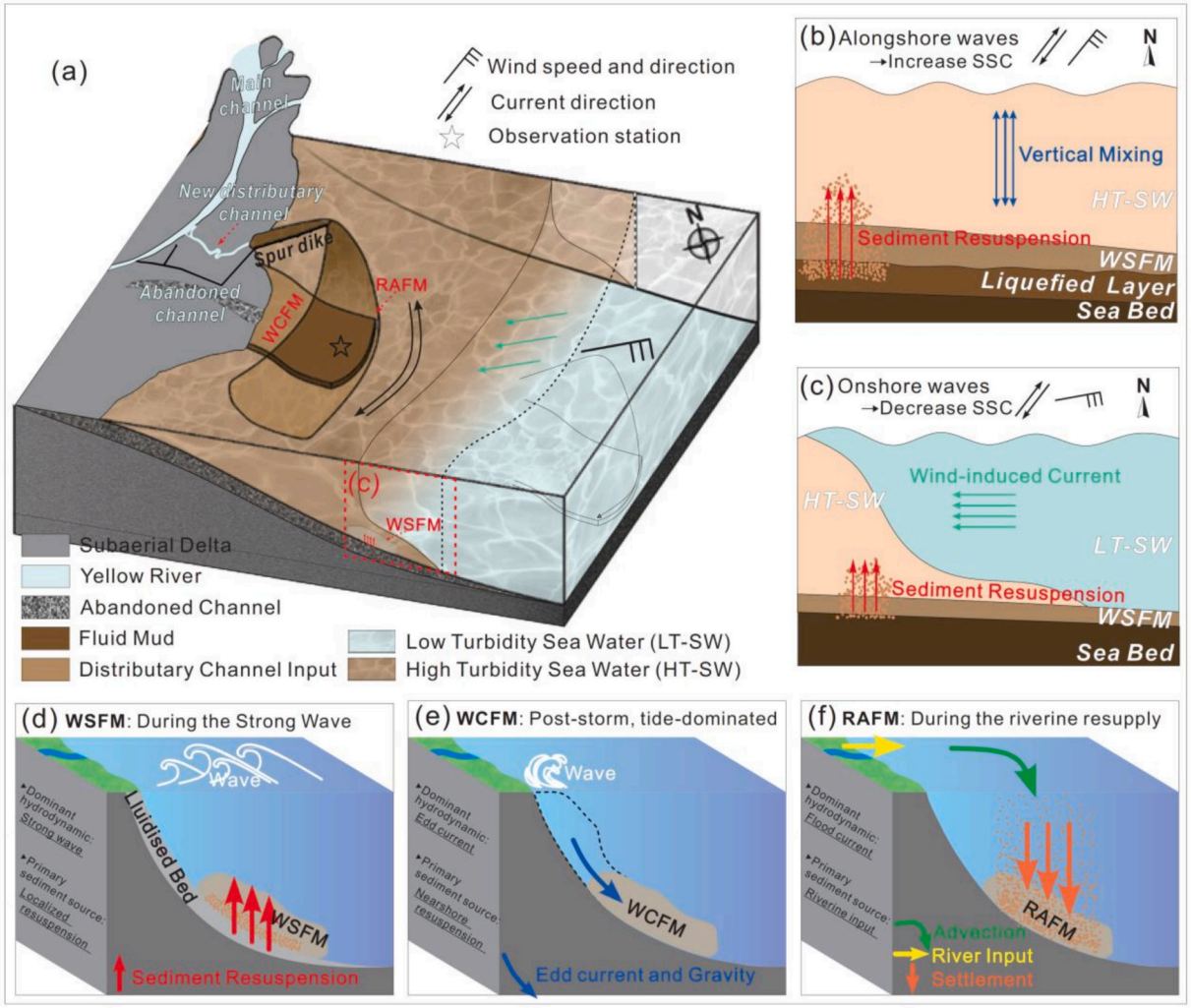


Fig. 8. (a) Mechanism diagram of the sedimentary dynamics of the SDAE; (b) Mechanism of SSC variation under alongshore wave action; (c) Mechanism of SSC variation under onshore wave action; (d) Schematic illustration of Wave-dominated Fluid Mud formation mechanisms; (e) Schematic illustration of Wave-current Coupled Fluid Mud formation mechanisms; (f) Schematic illustration of Riverine advection Fluid Mud formation mechanisms. The possible occurrence sites of the three FM types shown in Fig. 8a are for illustration purposes only and do not indicate that all three types can occur simultaneously.

across global delta systems, particularly in light of the increasing frequency of extreme weather events.

As an extreme manifestation of high SSC, FM exhibits formation mechanisms that vary markedly across estuarine deltas and are closely tied to site-specific sedimentary processes (Winterwerp, 2002; Hale and Ogston, 2015; Ge et al., 2020). In this study, we identified three characteristic types of FM in the SDAE of the Yellow River: Wave-Supported, Wave-current Coupled, and Riverine-Advected (Fig. 8d-f). Among these, WSFM functions as an efficient near-bed sediment transport mechanism commonly developed in high wave energy deltas, such as the Yangtze (Li et al., 2023a, 2023b) and Waipaoa (Hale and Ogston, 2015), where it plays a significant role in sediment transport and geomorphological evolution. In contrast, the occurrence of WCFM, which is not directly wave supported, suggests that the influence of strong waves on sediment transport in the SDAE is sustained beyond periods of active wave forcing. This coupled mechanism, involving initial wave-induced erosion followed by tide-driven transport, may represent a key pathway for post-storm sediment redistribution in the SDAE.

In this study, development of RAFM was also observed in the SDAE of the Yellow River. RAFM commonly occurs in active deltas receiving substantial riverine sediment input, such as the Severn (Manning et al., 2010), Yangtze (Wu et al., 2023), and Weser estuaries (Becker et al., 2013). In tide-dominated estuaries, RAFM is primarily driven by tidal asymmetry, persistent maximum turbidity zones, and continuous tidal pumping, making it a highly periodic, tidally-dominated process (Wu et al., 2022, 2023). And in river-dominated estuaries, RAFM development is primarily dependent on large-scale sediment inputs during riverine flood events (Wu et al., 2015; Luo et al., 2022; Li et al., 2023a). In contrast, the RAFM observed in the SDAE is not generated by a stable maximum turbidity zone or sustained riverine sediment supply, but is instead a direct response to a single Yellow River water and sediment regulation event, modulated by secondary distributary and flood tides, its fundamental control is event-driven rather than periodic. This finding indicats that under certain conditions(e.g., new secondary distributary development and favorable tidal transport), an abandoned estuarine delta can once again receive river re-supply and intermittent revert to sediment dynamic processes similar to those in active deltas, such as sediment sink in summer and sediment source in winter (Yang et al., 2011). According to the latest findings of Wang et al. (2025), river-dominated and wave-dominated deltas—especially those associated with large river systems—demonstrate heightened responsiveness to changes in fluvial sediment supply. Therefore, the riverine resupply in the SDAE of the Yellow River is expected to substantially enhance sediment supply, potentially mitigating—and in some cases even reversing—ongoing erosion in the subaqueous delta.

And the occurrence of RAFM during the S2 stage demonstrates that the study area resumed receiving sediment discharge from the Yellow River 28 years after the river's course was diverted in 1996. This finding suggests that not all deltas of abandoned estuaries are inevitably doomed to degradation. Beyond the SDAE of the Yellow River, several other deltas—including the western sector of the Parnaiba and the Ganges-Brahmaputra-Meghna delta (da Silva et al., 2019; Brown and Hale, 2022) and the southeast and northwest abandoned lobes of the Indus delta (Giosan et al., 2006), have also experienced episodic or periodic sediment resupply through autogenic reorganization, such as the formation of new distributary systems and hydrodynamic processes (tidal or wave action), which substantially mitigate local erosion. The riverine resupply offers in the SDAE of the Yellow River offered a valuable comparative example and conceptual framework for understanding the evolution of globally abandoned estuarine deltas following channel diversion. Moreover, the finding highlights that even episodic or localized riverine resupply can be a critical factor in shaping the long-term morphodynamic trajectory of SDAEs, and that its mechanisms warrant further investigation at the global scale.

While this study advances our understanding of sediment dynamics and controlling mechanisms in SDAEs across diverse depositional regimes using situ observations. Nevertheless, the inherent spatiotemporal limitations of situ observations constrain our current understanding of sediment transport pathways and the long-term morphodynamic evolution of SDAEs, particularly under the combined influences of strong wave activities and new secondary distributary. Future studies integrating numerical modeling and remote sensing approaches will enable a more comprehensive evaluation of how climate change and anthropogenic activities jointly influence the sediment dynamics and morphodynamic evolution of SDAEs.

5. Conclusion

Based on in-situ bottom boundary layer observations conducted during spring and summer in the subaqueous delta of the abandoned Yellow River estuary, we systematically analyzed the variation patterns and controlling mechanisms of SSC in the region. Results indicate that this region is predominantly governed by the combined influence of strong wave activity and episodic riverine re-supply associated with the newly developed secondary distributary channel. Strong wave activity enhances sediment resuspension and triggers bed liquefaction, serving as the principal driver of high SSC events. Furthermore, waves from different directions affect SSC through contrasting mechanisms, either intensifying hydrodynamics to promote sediment resuspension or reducing SSC via water mass exchange. Following river avulsion, the newly developed secondary distributary channel enables the SDAE to receive renewed fluvial sediment supply, resulting in markedly elevated SSC, particularly during water and sediment regulation events. Additionally, based on sediment provenance and prevailing hydrodynamic conditions, three types of FM were observed: wave-supported, wave-current-coupled, and riverine-advection, and their formation mechanisms were systematically addressed. Overall, we systematically elucidated the joint controlling effects of strong wave activity from different directions and episodic fluvial sediment re-supply via a new secondary distributary on the sedimentary dynamic of high SSC events and FM development in the subaqueous delta of the Yellow River estuary. These findings advance the mechanistic understanding of sediment transport processes in this region and provide important theoretical guidance for reassessing the global evolutionary trends and environmental changes in abandoned or sediment-starved deltas.

Open research

All data from this paper are publicly available at https://doi.org/10.5281/zenodo.15671242 and can also be found by contacting Longhai Zhu at zhulonghai@ouc.edu.cn.

CRediT authorship contribution statement

Chaoran Lin: Writing – original draft, Visualization, Investigation. **Longhai Zhu:** Writing – original draft, Supervision, Methodology. **Yaping Wang:** Writing – review & editing, Methodology. **Rui Bao:** Writing – review & editing, Visualization, Conceptualization. **Rijun Hu:** Writing – review & editing, Investigation. **Lingpeng Meng:** Writing – original draft, Methodology.

Declaration of competing interest

The authors declare that they have no known competing financial interests or personal relationships that could have appeared to influence the work reported in this paper.

Acknowledgements

This study was financially supported by the National Natural Science Foundation of China (NSFC, No.42276172).We would like to thank Editage (www.editage.cn) for English language editing.

Data availability

All data from this paper are publicly available at https://doi.org/10.5281/zenodo.15671242 and can also be found by contacting Longhai Zhu at zhulonghai@ouc.edu.cn.

References

Aleskerova, A., Kubryakov, A., Goryachkin, Y., Stanichny, S., Garmashov, A., 2019. Suspended-Matter distribution near the Western Coast of Crimea under the Impact of strong Winds of various Directions. Izv. Atmos. Ocean. Phys. 55, 1138–1149. https://doi.org/10.1134/S0001433819090044.

Baeye, M., Fettweis, M., Voulgaris, G., Lancker, V., 2011. Sediment mobility in response to tidal and wind-driven flows along the Belgian inner shelf, southern North Sea. Ocean Dyn. 61, 611–622. https://doi.org/10.1007/s10236-010-0370-7.

Becker, M., Schrottke, K., Bartholomä, A., Ernstsen, V., Winter, C., Hebbeln, D., 2013. Formation and entrainment of fluid mud layers in troughs of subtidal dunes in an estuarine turbidity zone. J. Geophys. Res. Oceans 118 (4), 2175–2187. https://doi.org/10.1002/jgrc.20153.

Becker, M., Maushake, C., Winter, C., 2018. Observations of mud-induced periodic stratification in a hyperturbid estuary. Geophys. Res. Lett. 45 (11), 5461–5469. https://doi.org/10.1029/2018GL077966.

Besset, M., Anthony, E., Bouchette, F., 2019. Multi-decadal variations in delta shorelines and their relationship to river sediment supply: an assessment and review. Earth Sci. Rev. 193, 199–219. https://doi.org/10.1016/j.earscirev.2019.04.018.

Bi, N., Yang, Z., Wang, H., Hu, B., Ji, Y., 2010. Sediment dispersion pattern off the present Huanghe (Yellow River) subdelta and its dynamic mechanism during normal river discharge period. Estuar. Coast. Shelf Sci. 86 (3), 352–362. https://doi.org/10.1016/j.ecss.2009.06.005.

Brand, A., Lacy, J., Hsu, K., Hoover, D., Gladding, S., Stacey, M.T., 2010. Wind-enhanced resuspension in the shallow waters of South San Francisco Bay: mechanisms and potential implications for cohesive sediment transport. J. Geophys. Res. Oceans 115 (C11). https://doi.org/10.1029/2010JC006172.

Brown, K., Hale, P., 2022. Persistence of depositional features in a strongly seasonal, tide-dominated delta. Estuar. Coast. Shelf Sci. 267, 107648. https://doi.org/10.1016/j.ecss.2021.107648.

Burchard, H., Schuttelaars, H.M., Ralston, D.K., 2018. Sediment trapping in estuaries. Annu. Rev. Mar. Sci. 10 (1), 371–395. https://doi.org/10.1146/annurev-marine-010816-060535.

Caldwell, R., Edmonds, D., Baumgardner, S., Paola, C., Roy, S., Nienhuis, J., 2019. A global delta dataset and the environmental variables that predict delta formation on marine coastlines. Earth Surf. Dyn. 7 (3), 773–787. https://doi.org/10.5194/esurf-7-773-2019.

Chadwick, A.J., Steele, S., Silvestre, J., Lamb, M.P., 2022. More extensive land loss expected on coastal deltas due to rivers jumping course during sea-level rise. Proc. Natl. Acad. Sci. 119 (31), e2119333119. https://doi.org/10.1073/pnas.2119333119.

Chen, Q., Wang, L., Tawes, R., 2008a. Hydrodynamic response of northeastern Gulf of Mexico to hurricanes. Estuar. Coasts 31, 1098–1116. https://doi.org/10.1007/s12237-008-9089-9.

Chen, X., Chen, S., Dong, P., Li, X., 2008b. Temporal and spatial evolution of the coastal profiles along the Yellow River Delta over last three decades. GeoJournal 71, 185–199. https://doi.org/10.1007/s10708-008-9155-7.

Colosimo, I., de Vet, P., van Maren, D., Reniers, A., Winterwerp, J., van Prooijen, C., 2020. The impact of wind on flow and sediment transport over intertidal flats. J Mar Sci Eng 8 (11), 910. https://doi.org/10.3390/jmse8110910.

da Silva, A.G.A., Stattegger, K., Vital, H., Schwarzer, K., 2019. Coastline change and offshore suspended sediment dynamics in a naturally develo** delta (Parnaíba Delta, NE Brazil). Mar. Geol. 410, 1–15. https://doi.org/10.1016/j.margeo.2018.12.013.

Darby, S., Hackney, C., Leyland, J., Kummu, M., Lauri, H., Parsons, D., Aalto, R., 2016. Fluvial sediment supply to a mega-delta reduced by shifting tropical-cyclone activity. Nature 539 (7628), 276–279. https://doi.org/10.1038/nature19809.

Egan, G., Cowherd, M., Fringer, O., Monismith, S., 2019. Observations of near-bed shear stress in a shallow, wave-and current-driven flow. J. Geophys. Res. Oceans 124 (8), 6323–6344. https://doi.org/10.1029/2019JC015165.

Fan, Y., Chen, S., Pan, S., Dou, S., 2020. Storm-induced hydrodynamic changes and seabed erosion in the littoral area of Yellow River Delta: a model-guided mechanism study. Cont. Shelf Res. 205, 104171. https://doi.org/10.1016/j.csr.2020.104171.

Fan, H., Yan, H., Teng, L., Liu, R., Li, Z., Cheng, H., Zhang, E., 2023. The effects of extreme flood events on the turbidity maximum zone in the Yangtze (Changjiang) Estuary. China. Mar. Geol. 456, 106993. https://doi.org/10.1016/j.margeo.2023.106993.

Fettweis, M., Francken, F., Van den Eynde, D., Verwaest, T., Janssens, J., Van Lancker, V., 2010. Storm influence on SPM concentrations in a coastal turbidity maximum area with high anthropogenic impact (southern North Sea). Cont. Shelf Res. 30 (13), 1417–1427. https://doi.org/10.1016/j.csr.2010.05.001.

Gao, J., Li, M., Chen, X., Li, C., Burrows, R., 2016, April. Numerical study on sediment concentration in Yellow river estuary. In: OCEANS 2016-Shanghai. IEEE, pp. 1–5.

Ge, J., Chen, C., Wang, Z., Ke, K., Yi, J., Ding, P., 2020. Dynamic response of the fluid mud to a tropical storm. J. Geophys. Res. Oceans 125 (3), e2019JC015419. https://doi.org/10.1029/2019JC015419.

Giosan, L., Constantinescu, S., Clift, P., Tabrez, A., Danish, M., Inam, A., 2006. Recent morphodynamics of the Indus delta shore and shelf. Cont. Shelf Res. 26 (14), 1668–1684. https://doi.org/10.1016/j.csr.2006.05.009.

Giosan, L., Syvitski, J., Constantinescu, S., Day, J., 2014. Climate change: protect the world's deltas. Nature 516 (7529), 31–33. https://doi.org/10.1038/516031a.

Gordon, L., Lohrmann, A., 2002. Near-shore Doppler current meter wave spectra. In Ocean Wave Measure. Anal. 33-43. https://doi.org/10.1061/40604(273)4.

Goring, D., Nikora, V., 2002. Despiking acoustic Doppler velocimeter data. J. Hydraul. Eng. 128 (1), 117–126. https://doi.org/10.1061/(ASCE)0733-9429(2002)128:1(117).

Grant, W., Madsen, O., 1979. Combined wave and current interaction with a rough bottom. J. Geophys. Res. Oceans 84 (C4), 1797–1808.

Guan, Q., Feng, L., Tang, J., Park, E., Ali, T.A., Zheng, Y., 2022. Trends in river total suspended sediments driven by dams and soil erosion: a comparison between the Yangtze and Mekong rivers. Water Resour. Res. 58 (10), e2022WR031979. https://doi.org/10.1029/2022WR031979.

Hale, R., Ogston, A., 2015. In situ observations of wave-supported fluid-mud generation and deposition on an active continental margin. J. Geophys. Res. Earth 120 (11), 2357–2373. https://doi.org/10.1002/2015JF003630.

Hou, X., Xie, D., Feng, L., Shen, F., Nienhuis, J.H., 2024. Sustained increase in suspended sediments near global river deltas over the past two decades. Nat. Commun. 15 (1), 3319. https://doi.org/10.1038/s41467-024-47598-6.

Jia, Y., Zhang, L., Zheng, J., Liu, X., Jeng, D.S., Shan, H., 2014. Effects of wave-induced seabed liquefaction on sediment re-suspension in the Yellow River Delta. Ocean Eng. 89, 146–156. https://doi.org/10.1016/j.oceaneng.2014.08.004.

Kineke, G., Sternberg, R., 1992. Measurements of high concentration suspended sediments using the optical backscatterance sensor. Mar. Geol. 108 (3–4), 253–258. https://doi.org/10.1016/0025-3227(92)90199-R.

Li, B., Jia, Y., Liu, J., Su, J., Liu, X., Wen, M., 2020. The controlling factors of high suspended sediment concentration in the intertidal flat off the Huanghe River Estuary. Acta Oceanol. Sin. 39 (10), 96–106. https://doi.org/10.1007/s13131-020-1679-9.

Li, L., Wang, J., Zheng, Y., Yao, Y., Guan, W., 2023a. Fluid mud dynamics and its correlation to hydrodynamics in Jiaojiang River Estuary, China. Ocean Sci. J. 58 (1), 8. https://doi.org/10.1007/s12601-023-00102-5.

Li, W., Li, M., Zhang, X., Li, J., 2023b. Characteristics of fluid mud in the Yangtze Estuary: storm, tide, and slope-triggered sediment dynamics and effects. Estuar. Coast. Shelf Sci. 281, 108194. https://doi.org/10.1016/j.ecss.2022.108194.

Liang, M., Liu, J., Lin, Y., He, Z., Wei, W., Jia, L., 2023. Typhoon-induced suspended sediment dynamics in the mouth-bar region of a river/wave-dominated estuary. Mar. Geol. 456, 106972. https://doi.org/10.1016/j.margeo.2022.106972.

Lin, C., Bao, R., Zhu, L., Hu, R., Ji, J., Yu, S., 2024. Surface sediment erosion characteristics and influencing factors in the subaqueous delta of the abandoned Yellow River Estuary. Mar. Geol. 468, 107219. https://doi.org/10.1016/j.margeo.2024.107219.

Liu, X., Zhang, H., Zheng, J., Guo, L., Jia, Y., Bian, C., Li, M., Ma, L., Zhang, S., 2020. Critical role of wave–seabed interactions in the extensive erosion of Yellow River estuarine sediments. Mar. Geol. 426, 106208. https://doi.org/10.1016/j.margeo.2020.106208.

Liu, X., Lu, Y., Yu, H., Ma, L., Li, X., Li, W., Zhang, H., Bian, C., 2022. In-situ observation of storm-induced wave-supported fluid mud occurrence in the subaqueous yellow river delta. J. Geophys. Res. Oceans 127 (7), e2021JC018190. https://doi.org/10.1029/2021JC018190.

Llebot, C., Rueda, F., Solé, J., Artigas, M., Estrada, M., 2014. Hydrodynamic states in a wind-driven microtidal estuary (Alfacs Bay). J. Sea Res. 85, 263–276. https://doi.org/10.1016/j.seares.2013.05.010.

Luo, W., Shen, F., He, Q., Cao, F., Zhao, H., Li, M., 2022. Changes in suspended sediments in the Yangtze River Estuary from 1984 to 2020: responses to basin and estuarine engineering constructions. Sci. Total Environ. 805, 150381. https://doi.org/10.1016/j.scitotenv.2021.150381.

Manning, A., Langston, W., Jonas, P., 2010. A review of sediment dynamics in the Severn Estuary: influence of flocculation. Mar. Pollut. Bull. 61 (1–3), 37–51. https://doi.org/10.1016/j.marpolbul.2009.12.012.

Mentaschi, L., Vousdoukas, M., Pekel, J., Voukouvalas, E., Feyen, L., 2018. Global long-term observations of coastal erosion and accretion. Sci. Rep. 8 (1), 1–11. https://doi.org/10.1038/s41598-018-30904-w.

Nicholls, R., Adger, W., Hutton, C., Hanson, S., 2020. Delta Challenges and Trade-Offs from the Holocene to the Anthropocene BT-Deltas in the Anthropocene. Springer International Publishing, Cham, Germany, pp. 1–22.

Nienhuis, J., Ashton, A., Roos, P., Hulscher, S., Giosan, L., 2013. Wave reworking of abandoned deltas. Geophys. Res. Lett. 40 (22), 5899–5903. https://doi.org/10.1002/2013GL058231.

Nienhuis, J., Ashton, A., Edmonds, D., Hoitink, A., Kettner, A., Rowland, J., Törnqvist, T., 2020. Global-scale human impact on delta morphology has led to net land area gain. Nature 577 (7791), 514–518. https://doi.org/10.1038/s41586-019-1905-9.

Niu, J., Xu, J., Li, G., Dong, P., Shi, J., Qiao, L., 2020. Swell-dominated sediment re-suspension in a silty coastal seabed. Estuar. Coast. Shelf Sci. 242, 106845. https://doi.org/10.1016/j.ecss.2020.106845.

Pawlowicz, R., Beardsley, B., Lentz, S., 2002. Classical tidal harmonic analysis including error estimates in MATLAB using T_TIDE. Comput. Geosci. 28 (8), 929–937. https://doi.org/10.1016/S0098-3004(02)00013-4.

Pelling, H., Uehara, K., Green, J., 2013. The impact of rapid coastline changes and sea level rise on the tides in the Bohai Sea, China. J. Geophys. Res. Oceans 118 (7), 3462–3472. https://doi.org/10.1002/jgrc.20258.

Qiu, Z., Xiao, C., Perrie, W., Sun, D., Wang, S., Shen, H., Yang, D., He, Y., 2017. Using Landsat 8 data to estimate suspended particulate matter in the Yellow River estuary. J. Geophys. Res. Oceans 122 (1), 276–290. https://doi.org/10.1002/2016JC012412.

Ross, M., Mehta, A., 1989. On the mechanics oflutoclines and fluid mud. J. Coast. Res. 5, 51–62. https://doi.org/10.2307/25735365.

Schmidt, F., Hinrichs, K., Elvert, M., 2010. Sources, transport, and partitioning of organic matter at a highly dynamic continental margin. Mar. Chem. 118 (1–2), 37–55. https://doi.org/10.1016/j.marchem.2009.10.003.
Shi, X., Hu, L., Qiao, S., Bai, Y., 2016. Progress in research of sedimentary organic carbon in the East China Sea: sources, dispersal and sequestration. Adv. Mar. Sci. 34 (3), 313–327.
Sobey, R., Hughes, S., 1999. A locally nonlinear interpretation of PUV measurements. Coast. Eng. 36 (1), 17–36. https://doi.org/10.1016/S0378-3839(98)00047-7.
Syvitski, J., Kettner, A., Overeem, I., Hutton, E., Hannon, M., Brakenridge, G., Giosan, L., Nicholls, R.J., 2009. Sinking deltas due to human activities. Nat. Geosci. 2 (10), 681–686. https://doi.org/10.1038/ngeo629.
Tang, J., Wang, Y., Zhu, Q., Jia, J., Xiong, J., Cheng, P., Wu, H., Chen, D., Wu, H., 2019. Winter storms induced high suspended sediment concentration along the north offshore seabed of the Changjiang estuary. Estuar. Coast. Shelf Sci. 228, 106351. https://doi.org/10.1016/j.ecss.2019.106351.
Tang, J., Wu, H., Xing, F., Zhang, F., Tang, B., Li, G., Wang, Y., 2023. Formation and transport of fluid mud triggered by typhoon events in front of the subaqueous Changjiang Delta. Mar. Geol. 460, 107052. https://doi.org/10.1016/j.margeo.2023.107052.
Tessler, Z., Vörösmarty, C., Grossberg, M., Gladkova, I., Aizenman, H., Syvitski, J., Foufoula-Georgiou, E., 2015. Profiling risk and sustainability in coastal deltas of the world. Science 349 (6248), 638–643. https://doi.org/10.1016/j.scitotenv.2021.150624.
Villaret, C., Trowbridge, J., 1991. Effects of stratification by suspended sediments on turbulent shear flows. J. Geophys. Res. Oceans 96 (C6), 10659–10680. https://doi.org/10.1029/91JC01025.
Wang, H., Wu, X., Bi, N., Li, S., Yuan, P., Wang, A., Nittrouer, J., 2017. Impacts of the dam-orientated water-sediment regulation scheme on the lower reaches and delta of the Yellow River (Huanghe): a review. Glob. Planet. Chang. 157, 93–113. https://doi.org/10.1016/j.gloplacha.2017.08.005.
Wang, Y., Peng, Y., Du, Z., Lin, H., Yu, Q., 2020. Calibrations of suspended sediment concentrations in high-turbidity waters using different in situ optical instruments. Water 12 (11), 3296. https://doi.org/10.3390/w12113296.
Wang, J., Chu, A., Dai, Z., Nienhuis, J., 2024. Delft3D model-based estuarine suspended sediment budget with morphodynamic changes of the channel-shoal complex in a mega fluvial-tidal delta. Eng. Appl. Comput. Fluid Mech. 18 (1), 2300763. https://doi.org/10.1080/19942060.2023.2300763.
Wang, J., Dai, Z., Mei, X., Duan, H.F., Nienhuis, J.H., 2025. Response time of global deltas to changes in fluvial sediment supply. Nat. Commun. 16 (1), 5573. https://doi.org/10.1038/s41467-025-60531-9.
Weeks, A., Simpson, J., Bowers, D., 1993. The relationship between concentrations of suspended particulate material and tidal processes in the Irish Sea. Cont. Shelf Res. 13 (12), 1325–1334. https://doi.org/10.1016/0278-4343(93)90086-D.
Whitehouse, R., 2000. Dynamics of Estuarine Muds. Thomas Telford.
Winterwerp, H., 1999. On the dynamics of high-concentrated mud suspensions. Commun. Hydraul. Geotech. Eng. 171.
Winterwerp, J.C., 2002. On the flocculation and settling velocity of estuarine mud. Cont. Shelf Res. 22 (9), 1339–1360. https://doi.org/10.1016/S0278-4343(02)00010-9.
Wu, Z., 1994. Estimate approached of ηUV, PUV and UV directional wave spectra and their comparison. Ocean Eng. 12, 79–86.
Wu, X., Bi, N., Yuan, P., Li, S., Wang, H., 2015. Sediment dispersal and accumulation off the present Huanghe (Yellow River) delta as impacted by the Water-Sediment Regulation Scheme. Cont. Shelf Res. 111, 126–138. https://doi.org/10.1016/j.csr.2015.11.003.
Wu, H., Wang, Y.P., Gao, S., Xing, F., Tang, J., Chen, D., 2022. Fluid mud dynamics in a tide-dominated estuary: a case study from the Yangtze River. Cont. Shelf Res. 232, 104623. https://doi.org/10.1016/j.csr.2021.104623.
Wu, H., Tang, J., Li, W., Xing, F., Yang, H., Zhang, F., Wang, Y., 2023. Fluid mud induced by periodic tidal advection and fine-grained sediment settling in the Yangtze estuary. Front. Mar. Sci. 10, 1323692. https://doi.org/10.3389/fmars.2023.1323692.
Xing, G., Wang, H., Yang, Z., Bi, N., 2016. Spatial and temporal variation in erosion and accumulation of the subaqueous Yellow River Delta (1976–2004). J. Coast. Res. 74, 32–47. https://doi.org/10.2112/SI74-004.1.
Yang, Z., Ji, Y., Bi, N., Lei, K., Wang, H., 2011. Sediment transport off the Huanghe (Yellow River) delta and in the adjacent Bohai Sea in winter and seasonal comparison. Estuar. Coast. Shelf Sci. 93 (3), 173–181. https://doi.org/10.1016/j.ecss.2010.06.005.
Yang, Y., Chen, S., Xu, C., 2021. Morphodynamics and tidal flow asymmetry of the Huanghe River Estuary. Haiyang Xuebao 43 (6), 13–25. https://doi.org/10.12284/hyxb2021094.
Yao, H., Liu, X., Li, M., Li, W., Song, Y., Tan, Z., Shetaia, S.A., 2024. Effect of typhoon on suspended sediment concentration, bed erosion and sediment transport in the Yangtze Estuary. Mar. Geol. 475, 107357. https://doi.org/10.1016/j.margeo.2024.107357.
Yunus, A., Masago, Y., Boulange, J., Hijioka, Y., 2022. Natural and anthropogenic forces on suspended sediment dynamics in Asian estuaries. Sci. Total Environ. 836, 155569. https://doi.org/10.1016/j.scitotenv.2022.155569.
Zeng, W., Dai, Z., Luo, J., Lou, Y., Mei, X., 2024. Morphodynamics of the dredged channel in a mega fluvial-tidal delta. J. Hydrol. 639, 131592. https://doi.org/10.1016/j.jhydrol.2024.131592.
Zhang, S., Zhang, Y., Xu, J., Guo, L., Li, G., Jia, Y., Zhu, C., 2022. In situ observations of hydro-sediment dynamics on the abandoned Diaokou lobe of the Yellow River Delta: erosion mechanism and rate. Estuar. Coast. Shelf Sci. 277, 108065. https://doi.org/10.1016/j.ecss.2022.108065.
Zheng, S., Han, S., Tan, G., Xia, J., Wu, B., Wang, K., Edmonds, D.A., 2018. Morphological adjustment of the Qingshuigou channel on the Yellow River Delta and factors controlling its avulsion. Catena 166, 44–55. https://doi.org/10.1016/j.catena.2018.03.009.
Zhou, L., Liu, J., Saito, Y., Diao, S., Gao, M., Qiu, J., Ye, S., 2020. Sediment budget of the Yellow River delta during 1959–2012, estimated from morphological changes and accumulation rates. Mar. Geol. 430, 106363. https://doi.org/10.1016/j.margeo.2020.106363.
Zhu, Q., Xing, F., Wang, Y.P., Syvitski, J., Overeem, I., Guo, J., Gao, S., 2024. Hidden delta degradation due to fluvial sediment decline and intensified marine storms. Sci. Adv. 10 (18), eadk1698. https://doi.org/10.1126/sciadv.adk1698.